

Variable Radiance Field for Real-Life Category-Specific Reconstruction from Single Image

Kun Wang, Zhiqiang Yan, Zhenyu Zhang, Xiang Li, Jun Li, and Jian Yang

Abstract—Reconstructing category-specific objects from a single image is a challenging task that requires inferring the geometry and appearance of an object from a limited viewpoint. Existing methods typically rely on local feature retrieval based on re-projection with known camera intrinsic, which are slow and prone to distortion at viewpoints distant from the input image. In this paper, we present Variable Radiance Field (VRF), a novel framework that can efficiently reconstruct category-specific objects from a single image without known camera parameters. Our key contributions are: (1) We parameterize the geometry and appearance of the object using a multi-scale global feature extractor, which avoids frequent point-wise feature retrieval and camera dependency. We also propose a contrastive learning-based pretraining strategy to improve the feature extractor. (2) We reduce the geometric complexity of the object by learning a category template, and use hypernetworks to generate a small neural radiance field for fast and instance-specific rendering. (3) We align each training instance to the template space using a learned similarity transformation, which enables semantic-consistent learning across different objects. We evaluate our method on the CO3D dataset and show that it outperforms existing methods in terms of quality and speed. We also demonstrate its applicability to shape interpolation and object placement tasks.

Index Terms—Neural radiance field, 3D Reconstruction, Novel view synthesis, Contrastive learning.

I. INTRODUCTION

CREATING 3D objects from images has received increasing attention in 3D multimedia applications such as cultural heritage, education, training, tourism, and e-commerce [1]–[7]. These applications demand efficient and user-friendly methods for creating realistic 3D models. In recent years, Neural Radiance Field (NeRF) [8] has shown great promise on reconstructing high-quality 3D objects, although it requires many input images and consumes much time for instance-specific optimization. To address these limitations, several variants [9]–[12] of NeRF have been proposed that use image priors to infer the 3D structure of unseen objects from few images. These methods typically project the 3D points onto the input image planes using known camera parameters and retrieve local image features for each point. The features are then decoded to density and color values, which are used for volume rendering [13]. Generally, these methods can well render target views close to the input images.

Kun Wang, Zhiqiang Yan, Jun Li, and Jian Yang are with PCA-Lab, School of Computer Science and Engineering, Nanjing University of Science and Technology, Nanjing, China (e-mail: {kunwang, Yanzq, junli, csjyang}@njust.edu.cn).

Zhenyu Zhang is with Tencent YouTu Lab, Shanghai, China (e-mail: zhangjesse@foxmail.com).

Xiang Li is with Nankai University, Tianjin, China (e-mail: xiang.li.implus@njust.edu.cn).

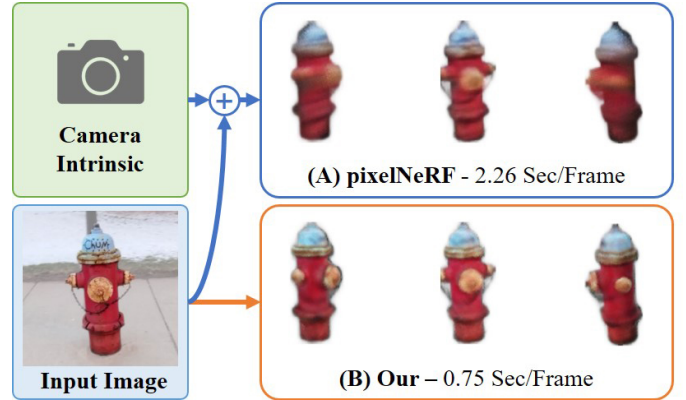


Fig. 1. (A) pixelNeRF [9] requires both image and known camera intrinsic as input and suffers from slow rendering. (B) Our method doesn't require any known camera parameter at inference time, and can efficiently render plausible novel views of reconstructed objects from only one image.

However, these methods face several challenges when applied to single-image reconstruction. Firstly, they assume that the input image has sufficient visual overlap with the target view, which may not hold for occluded regions, as shown in Fig. 2. Therefore, they struggle to reconstruct an object from a single input image. Secondly, rendering an image involves a large number of queries for spatial points, causing them to frequently retrieve and integrate image features, which slows down their rendering. Finally, they depend on the re-projection of the 3D points onto the input image plane using known camera intrinsic, which limits their applicability since accurate intrinsic for in-the-wild images are hard to acquire. To address these issues, we propose a novel NeRF-based framework that can efficiently reconstruct a category-specific object from single real-life image without requiring known camera parameters at inference time.

Our framework, which we call VRF, consists of three modules: parameterization, instance modeling and dynamic ray sampling. The parameterization module represents an object using global features, which enables us to discard frequent local feature retrieval and thus avoid the dependence on accurate camera intrinsic. Concretely, it extracts multi-level features from the input image using a convolutional feature extractor and integrates them into a latent representation that encodes the geometry and appearance of the object. We pre-train the feature extractor with contrastive learning [14]–[16], a self-supervised technique that learns to distinguish between different instances, to enhance its ability to capture useful features. The instance modeling module constructs an

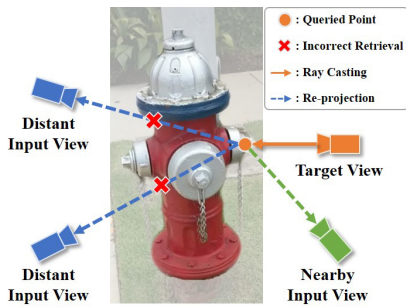


Fig. 2. The local feature retrieval can correctly sample local features from nearby input views. However, it often samples incorrect features from distant input views due to self-occlusions.

instance-specific radiance field that can be efficiently rendered from novel viewpoints. To reduce the geometric complexity, we learn a category-specific shape template that captures the common geometric features of the category and deform it with instance-specific deformations to create the instance shape. Moreover, we employ hypernetworks [17], which are neural networks that generate other neural networks as their outputs, to generate small instance-specific neural networks for fast rendering, avoiding the need for large category-specific models. The dynamic ray sampling module learns an instance-specific 3D similarity transformation to align each training object with the template. This is important for two reasons: 1) It ensures a consistent canonical space for instances within a category, which is crucial for semantic-consistent learning as real-life datasets (*e.g.* CO3D [18]) often have objects with different orientations. 2) It allows the instance shape to be created with less deformation, making better use of the shape prior of the template.

In short, our contributions can be summarized as follows:

- We parameterize an object with global features extracted from the input image at multiple levels, and pre-train the feature extractor with contrastive learning for better feature extraction.
- We model the object geometry with a category-specific template and instance-specific deformations to reduce the complexity, and use hypernetworks to generate small neural networks for efficient rendering.
- We learn a 3D transformation for each instance to align it with the template, enabling semantic-consistent learning.

By combining these contributions, our framework achieves state-of-the-art performance and faster rendering speed than existing methods on single-image category-specific reconstruction task. We also show that our method can be extended to various applications such as shape interpolation, object synthesis and object placement.

II. RELATED WORK

A. Category-Specific Reconstruction.

We review the related work on reconstructing a category-specific object from 2D images, which is a long-standing and well-studied task. Early methods used 3D supervision to learn the geometry and appearance of the object, and represented them in 3D space with various forms, such as

point clouds [19], meshes [20], voxel grids [21] and signed distance fields [22]. Later methods avoided the 3D supervision by using differentiable rendering based methods [23], [24]. These methods were mainly trained on synthetic datasets such as ShapeNet [25], which have simpler and more consistent objects than real-world datasets. Some other methods focused on learning from real-world datasets. CMR [26] proposed a learning framework to recover the shape, texture and camera of an object from a single image. U-CMR [27] introduced camera-multiplex to model the distribution over cameras. Dove [28] explored the method to learn deformable objects from monocular videos.

NeRF [8] has attracted much attention recently due to its remarkable performance on the reconstruction task. FiG-NeRF [29] extended NeRF to optimize the 3D representation of object categories by using a shape template. CodeNeRF [30] disentangled the shape and texture of objects and used an auto-decoder [31] architecture to model unseen objects. LOLNeRF [32] proposed to learn 3D structure from data with only single views of each object. However, these methods require independent optimization for each unseen object, which limits their practical application.

B. NeRF from Few Images.

Our work is related to previous approaches that can create NeRF from few images. One of the limitations of NeRF is the requirement for many input images. Several methods have addressed this problem by introducing semantic consistency loss [33], depth information from structure-from-motion method [34] and pre-trained depth completion model [35], data augmentation with geometric constraints [36], or semantic and geometry regularizations [37] to train NeRF from few images. However, these methods require independent optimization for each object or scene.

In contrast, some methods can predict the underlying 3D of unseen objects from few images without additional optimization. These methods rely on local image features to condition the density and color of spatial points, such as pixelNeRF [9], GRF [38], Henzler *et al.* [39], and NerFormer [18]. Other methods improve the reconstruction performance by using stereo cues [11], [40], geometry priors [12], or vision transformers [41]. Our method also reconstructs unseen objects without additional optimization, but uses global features to avoid incorrect feature sampling and camera dependency.

III. METHOD

In this section, we detail our framework, termed Variable Radiance Field (VRF). VRF consists of three modules: parameterization, instance modeling and dynamic ray sampling. Before elaborating these modules and introducing the training losses, we first present an overview of our framework.

A. Overview.

Our goal is to learn a generalizable radiance field model that, at inference time, can quickly reconstruct an object of specific category from only one image, then render it from

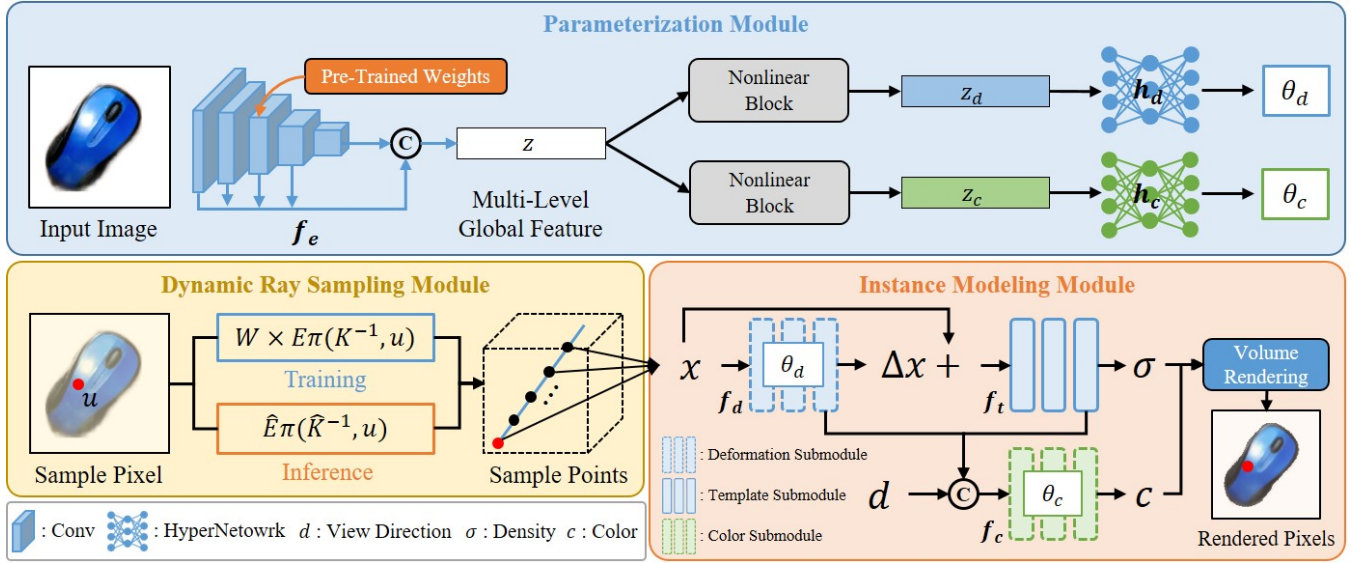


Fig. 3. The overall pipeline of our VRF framework. The feature extractor f_e is pre-trained based on a contrastive learning strategy, which is illustrated in Fig. 4. \odot denotes concatenation along channel dimension.

novel viewpoints. To train this model, we require a training dataset $\mathcal{C} = \{(I_i, M_i, E_i, K_i)\}_{i=1}^N$ of N color images $I_i \in \mathbb{R}^{3 \times H \times W}$, along with their foreground masks $M_i \in \mathbb{R}^{1 \times H \times W}$, camera poses $E_i \in SE(3)$ and intrinsics $K_i \in \mathbb{R}^{3 \times 3}$. Note that, E and K are only used in training to supervise the reconstruction and are no longer required at inference time.

The overall pipeline is shown in Fig. 3. Our framework consists three modules:

- The parameterization module extracts useful features z from the input image using a multi-level extractor f_d , and projects z to geometry and appearance representations z_d and z_c , which are used to generate network weights θ_d and θ_c by hypernetworks h_d and h_c .
- The instance modeling module models the instance geometry with category-specific template f_t and instance-specific deformations Δx estimated by f_d , and predicts the point color with f_c . f_d and f_c are two small Multi-Layer Perceptrons (MLPs) with generated weights θ_d and θ_c .
- The dynamic ray sampling module samples rays using known camera parameters E and K at training time and align them to template space using learned transformation W . During inference, it directly sample rays with customized camera parameters \hat{K} and \hat{E} .

In the following subsections, we will elaborate these three modules, then introduce the training losses.

B. Parameterization Module

The parameterization module Φ_p takes an image I and its foreground mask M as input, and generate two small MLPs with weights θ_d and θ_c for the instance modeling module, *i.e.*

$$\Phi_p : (I, M) \rightarrow (\theta_d, \theta_c). \quad (1)$$

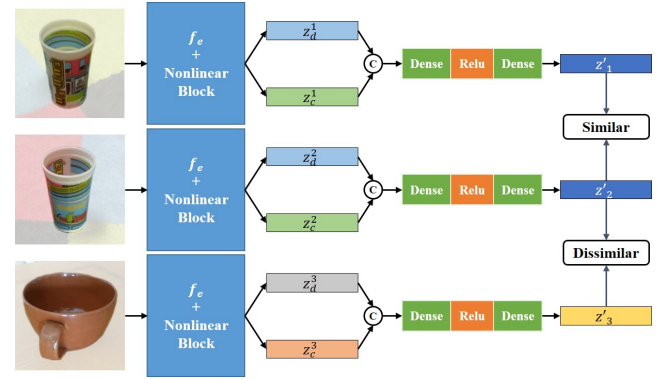


Fig. 4. An illustration of the contrastive learning-based strategy for pre-training the feature extractor f_e . f_e is trained to generate similar representations for images from the same instance and dissimilar representations for images from different instances.

1) *Parameterizing object properties:* We first parameterize the object properties from the input image pair (I, M) using a feature extractor f_e . The feature extractor f_e is a convolutional encoder that outputs multi-level features $z = f_e(I, M)$ at each layer. The features at different layers contain information of different semantic levels, so we concatenate them to form a comprehensive representation of the object properties. We then project z into two latent vectors z_d and z_c that encode the geometry and appearance of the object, respectively. The projection is done by two nonlinear blocks, each consisting of two linear layers and an intermediate LeakyRelu activation.

2) *Accelerating with hypernetworks:* We aim to generate an instance-specific radiance field by predicting the density and color of each spatial point x based on two latent vectors: z_d for deformation and z_c for color. A naive approach is to concatenate z_d and z_c with x and feed them into a large network that models the whole category. However, this is inefficient as it requires many predictions for different points

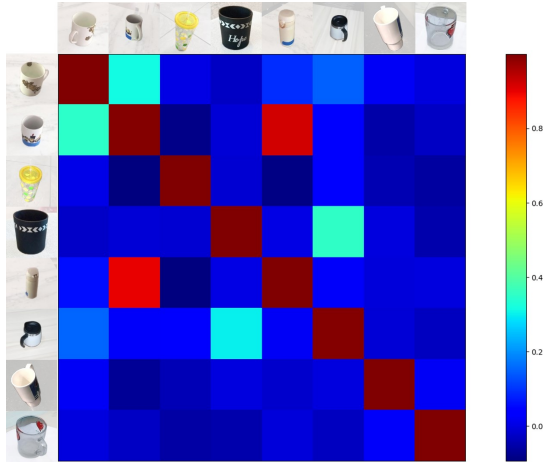


Fig. 5. After pre-training, the feature extractor f_e can produce similar representations from different input images of the same instance, and produce dissimilar representations for different instances.

to render an image. To address this issue, we propose a novel method that uses hypernetworks h_d and h_c to condition the radiance field generation. Given z_d and z_c , the hypernetworks produce the weights $\theta_d = h_d(z_d)$ and $\theta_c = h_c(z_c)$ for two small submodules that perform instance-level deformation and color predictions. This way, we can achieve fast and flexible rendering of diverse instances.

3) *Contrastive learning-based pre-training:* We pre-train the feature extractor f_e with a contrastive learning-based strategy, which introduces priors for better detecting object properties. Fig. 4 illustrates the overall idea of this strategy. First, we randomly select different instances within the same category and randomly sample two images from each instance with different viewpoints. Then, we concatenate the latent vectors z_d and z_c and project them to a low-dimensional representation z' . We train f_e to generate representations z' that are similar for different images of the same instance and dissimilar for different instances, using the NT-Xent loss proposed in SimCLR [15] as the supervision. As shown in Fig. 5, f_e can well distinguish between images from different views of the same instance and images from different instances after pre-training. This demonstrates that f_e has learned to extract useful features to detect object properties, which is beneficial for object reconstruction.

C. Instance Modeling Module

The instance modeling module Φ_i constructs a continuous radiance field for each instance. It predicts the density σ and color c for given spatial point x conditioned on z_d and z_c , respectively, *i.e.*

$$\Phi_i : x \rightarrow (\sigma, c). \quad (2)$$

The predicted densities and colors can be rendered to 2D images through volume rendering [13].

1) *Density prediction:* To reduce the modeling complexity of the geometry, we learn a shape template for each category and create the instance shape with instance-specific deformations. This is motivated by the observation that instances

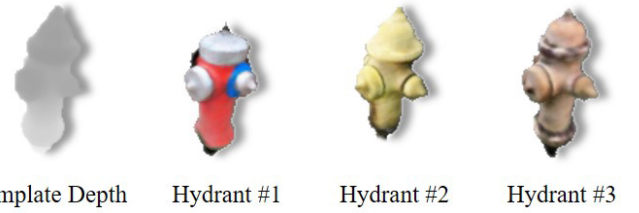


Fig. 6. Our framework learns to transform each instance to match the category-specific template, ensuring semantic consistency across different shapes. We render these three hydrants with the same camera parameters, showing that they have the similar orientation and scale.

within the same category often share similar geometries. However, we do not have any prior knowledge of the category geometry at the beginning of the training. Therefore, we start learning the template from an instance shape. Specifically, we randomly select an instance from each category and reconstruct it with a NeRF MLP. We then initialize the template submodule f_t with the weights of this MLP. During training, we fine-tune f_t to create instance shapes with less deformations to capture the common geometric features of the category. The deformation submodule $f_d : (x, \theta_d) \rightarrow \Delta x$ predicts the instance-specific deformation Δx for point x , using the weights generated by the hypernetwork h_d . Finally, the density σ of point x is predicted as follows:

$$\sigma = f_t(x + f_d(x, \theta_d)). \quad (3)$$

2) *Color prediction:* We predict the color c for point x using the color submodule f_c , which uses the weights generated by the hypernetwork h_c . The input of f_c consists of the view direction d and the feature maps F_d and F_t from the last layers of f_d and f_t , respectively. The view direction d handles the view-dependent appearance, while the feature maps F_d and F_t enrich the input information. We predict the color c of point x as follows:

$$c = f_c(F_d, F_t, d). \quad (4)$$

3) *Rendering:* The predicted σ and c along each ray r are composited into the pixel color $\hat{C}(r)$ via volume rendering:

$$\hat{C}(r) = \int_{t_n}^{t_f} T(t)\sigma(t)c(t)dt, \quad (5)$$

where $T(t) = \exp(-\int_{t_n}^t \sigma(s)ds)$ handles occlusions, and t_n and t_f are the near and far depth bounds, respectively.

D. Dynamic Ray Sampling Module

The dynamic ray sampling module Φ_s maps a pixel location u to a ray r that starts from o and goes through u with direction d , *i.e.*

$$\Phi_s : u \rightarrow (o, d). \quad (6)$$

This module operates in two modes: 1) In training mode, it uses the known camera parameters to generate rays and learns to transform them to the template space, ensuring semantic-consistent learning across different instances. 2) During inference, it samples rays from any desired viewpoint to render an instance from novel viewpoints. We will explain these two modes in more detail below.

1) *Training mode*: To train our model, we use the given camera pose E and intrinsic K to render a target view and compare it with the ground truth image I for supervision. However, real-life datasets, such as CO3D [18], have different instances with varying orientation and scale due to the global coordinate frame and scaling ambiguity [39], [42]. This causes semantic inconsistency and learning difficulty as the model has to account for these variations to render the target views correctly. To address this problem, we learn an instance-specific 3D similarity transformation $W \in S(3)$ to align each instance with the category-specific template space defined by f_t . Specifically, we first roughly unify the orientation and scale of each instance by matching their landmark points, which are obtained in a data preprocessing step (see the supplement). Then, we fine-tune W during training to minimize the deformations needed to create the instance shape. Finally, we generate the ray r by:

$$r \leftarrow W \times E\pi(K^{-1}, u), \quad (7)$$

where \times denotes matrix multiplication. This way, different instances within the same category have consistent orientation and scale, as shown in Fig. 6.

a) *Inference mode*: During inference, an object is reconstructed as an instance-specific radiance field in the template space. It can be efficiently rendered to images with user-defined camera poses \hat{E} and intrinsics \hat{K} , which are used to generate rays by $\hat{\Phi}_s$:

$$r \leftarrow \hat{E}\pi(\hat{K}^{-1}, u). \quad (8)$$

E. Training Loss

1) *Photometric loss*: We apply a weighted MSE loss to measure the error between rendered pixel $\hat{C}(r)$ and ground truth pixel $C(r)$ of each ray r :

$$L_p = \mathbb{E}_{r, \hat{C}, C}[w_t \|\hat{C}(r) - C(r)\|^2], \quad (9)$$

where w_t is a weight term that measures the viewpoint difference between r and the input image with cosine similarity. We assign more weight to the rays from near viewpoints, since the rays from very distant viewpoints are unpredictable.

2) *Foreground loss*: We define the binary mask $\hat{M} = [M > 0.5]$ using Iverson bracket $[\cdot]$ to mark foreground pixels. Specifically, we apply a weighted ℓ_1 loss to constrain the consistency between the ray opacity $\hat{O}(r)$ and the corresponding mask $\hat{M}(r)$:

$$L_f = \mathbb{E}_{\hat{O}, \hat{M}}[w_f \|\hat{O}(r) - \hat{M}\|_1], \quad (10)$$

where $w_f = |M - 0.5|$ is the confidence of $\hat{M}(r)$, and that ray opacity $\hat{O}(r)$ is defined as:

$$\hat{O}(r) = \int_{t_n}^{t_f} T(t)\sigma(t)dt. \quad (11)$$

3) *Deformation regularization*: To ensure that the shape template learns meaningful category geometry and the transformation W properly aligns each instance, we impose the ℓ_2 regularization to make the deformations Δx to be small:

$$L_r = \sum \|\Delta x\|_2^2. \quad (12)$$

Furthermore, we employ the point pair regularization introduced in [43] to avoid extreme distortion:

$$L_d = \sum_{m=1}^{N_p} \sum_{i \neq j} \max\left(\frac{\|\Delta x_i - \Delta x_j\|_2}{\|x_i - x_j\|_2} - \epsilon, 0\right), \quad (13)$$

where N_p is the number of sampled point pairs and ϵ is a parameter controlling the distortion tolerance.

4) *Final loss*: The final loss is the weighted summation of above losses:

$$L = L_p + \lambda_f L_f + \lambda_r L_r + \lambda_d L_d, \quad (14)$$

where λ_f , λ_r and λ_d are weight coefficients which are set to 0.4, 0.1 and 0.1, respectively, in our experiments.

IV. EXPERIMENT

We conduct experiments to evaluate the performance and effectiveness of our method on the task of single-image category reconstruction. We compare our method with existing state-of-the-art (SOTA) methods and show that our method achieves better quality and faster inference speed. We also perform ablation studies to analyze the impact of different components in our framework. Furthermore, we demonstrate the applicability of our method to various tasks such as shape interpolation and object placement. In this section, we first describe the experimental setup and implementation details, and then present the results and analysis.

A. Experimental Setup

We conduct our experiments on five categories of the CO3D [18] dataset: banana, cellphone, mouse, hydrant and cup. All experiments follow the official data split for training and testing. Since our goal is to reconstruct objects from a single image, we only use the first image of each test sample as the input and render the target image from the given viewpoint. We compare our framework with five related approaches: pixelNeRF [9], Henzler *et al.* [39], GRF [38], NerFormer [18] and VisionNeRF [41]. All approaches are separately trained on each category. We use three metrics to measure the reconstruction quality: PSNR, SSIM [44] and LPIPS [45]. PSNR measure pixel-wise error and favor mean color prediction while SSIM and LPIPS measure structural similarity and favor perceptual agreement. Note that, PSNR is only aggregated over the foreground pixels masked by M . In addition, we measure the average rendering time of different methods by rendering 100 images of 128×128 resolution on a single TITAN RTX GPU.

B. Implementation Detail

We implement our framework using Pytorch [46] and Pytorch3D [47]. We use a ResNet-18 [48] as the feature extractor f_e and remove the batch normalization [49] layers from it, since we found they were unstable when processing images that only kept the foreground. We set the dimensions of z_d and z_c to 512. We parameterize the 3D similarity transformation W with a 10-dimensional vector that consists of 6 elements for rotation, 3 elements for translation and 1 element for scaling.

TABLE I

QUANTITATIVE COMPARISON WITH EXISTING METHODS. OUR FRAMEWORK OUTPERFORMS EXISTING METHODS IN TERMS OF QUALITY AND SPEED.

Method	Sec/Frame	Banana			Mouse			Hydrant			Cellphone			Cup		
		PSNR \uparrow	SSIM \uparrow	LPIPS \downarrow	PSNR \uparrow	SSIM \uparrow	LPIPS \downarrow	PSNR \uparrow	SSIM \uparrow	LPIPS \downarrow	PSNR \uparrow	SSIM \uparrow	LPIPS \downarrow	PSNR \uparrow	SSIM \uparrow	LPIPS \downarrow
pixelNeRF [9]	2.26	20.161	0.503	0.401	18.696	0.395	0.474	15.773	0.605	0.346	16.882	0.460	0.432	16.976	0.381	0.521
Henzler <i>et al.</i> [39]	0.96	18.574	0.813	0.201	14.904	0.561	0.396	15.040	0.775	0.205	10.458	0.583	0.375	15.371	0.656	0.324
GRF [38]	1.65	22.858	0.688	0.310	21.029	0.563	0.398	17.670	0.788	0.235	19.673	0.644	0.353	19.387	0.556	0.418
NerFormer [18]	1.05	19.170	0.822	0.192	17.017	0.666	0.308	15.927	0.764	0.213	13.691	0.705	0.281	16.611	0.696	0.298
VisionNeRF [41]	2.19	12.086	0.772	0.269	11.852	0.473	0.421	10.216	0.641	0.298	9.991	0.532	0.401	10.196	0.488	0.430
Our	0.75	22.987	0.861	0.168	22.281	0.769	0.240	19.009	0.847	0.162	20.945	0.841	0.159	20.903	0.684	0.333

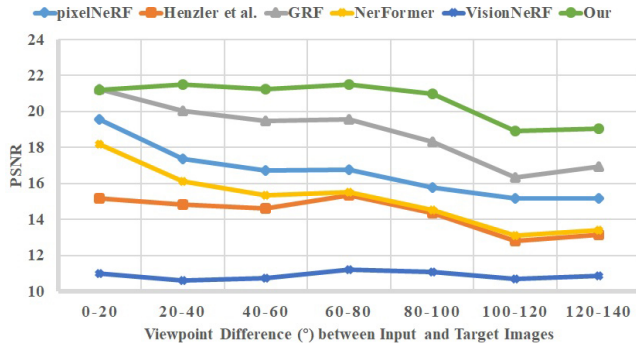


Fig. 7. Average PSNR results over five categories at different levels of viewpoint difference (°) between input and target images.

We represent the rotation with the continuous representation proposed in [50]. In Φ_i , we use MLPs with 192 hidden neurons and ELU [51] nonlinearities for all three submodules. The submodules f_d , f_t and f_c have 6, 8 and 3 linear layers, respectively. The hypernetworks h_d and h_c generate weights for each linear layer of f_d and f_c using a sub-hypernetwork that consists of a 3-layer MLP. The first two layers of the sub-hypernetwork have 512 and 48 neurons, respectively. We train a separate model for each object category using the Adam [52] optimizer for 1200 epochs. We use different initial learning rates for different components: $5e^{-5}$ for f_t , $1e^{-2}$ for W , $5e^{-4}$ for the hypernetworks, and $1e^{-4}$ for the rest. The learning rate is reduced to half every 400 epochs.

C. Comparison with Existing Methods

We report the quantitative results in TABLE. I. As shown in this table, our framework achieves superior performance and inference speed over the existing methods. Our method attains the highest PSNR values in all categories, for instance, it improves GRF by 7.58% on Hydrant. Our method also excels in SSIM and LPIPS metrics in four categories, except for Cup. This indicates that our method can reconstruct plausible geometry and appearance from a single image, without requiring additional camera parameters. Furthermore, our method renders a frame in the shortest time, for example, it reduces the rendering time by 66.81% compared with pixelNeRF. This demonstrates the effectiveness of our global representation design and hypernetwork-based acceleration strategy. To show the robustness of our method to the viewpoint of the input image, we group the test samples by the viewing angle difference between the input image and the target image, and compute the average PSNR metric for each group. Fig. 7 illustrates the

results. Our method maintains a stable performance when the viewing angle difference is less than 100° , and only degrades when the viewing angle difference is larger than 100° . In contrast, other methods, such as GRF and pixelNeRF, suffer from a significant performance drop when the viewing angle difference is less than 40° .

Fig. 8 shows the qualitative comparisons with existing methods. We use the input image (shown in the first column) to reconstruct the instance and render two novel views of it. The ground truth images are shown in the last two columns. For each category, we report the reconstruction results of two instances. Existing methods depend on local feature retrieval, which causes blurry and distorted results when the viewpoint is far from the input image, as seen in the Hydrant and the first Cup samples. Our method, on the other hand, uses global multi-level features, which result in sharper and 3D-consistent results. Moreover, thanks to the category-specific template and foreground loss, our method can generate novel views with clear boundaries between the fore- and back-ground, while other methods, such as GRF, produce novel views with unclear background, such as the first mouse sample.

D. Ablation Study

Here, we first demonstrate the effectiveness of each component in our framework through ablation study on banana category, and report the quantitative results in TABLE. II. We start with a baseline method and add the remained components one by one. The baseline method does not learn the transformation W to align each instance, and predicts the density σ of x directly without using the shape template. It also only uses the feature from the last layer of f_e . The first component we add is the category-specific template, which allows us to create the instance shape with instance-specific deformations. We report the result of this component as + *Template*. However, the performance decreases compared to the baseline method. We attribute this to the semantic-inconsistent learning, which is resolved by aligning each instance to the template space as + *Alignment*. This component significantly improves the performance over the baseline method. Next, we add the multi-level feature component as + *Multi-Level Feature*, which further boosts the performance by 1.0% in PSNR. Finally, we add the contrastive learning-based pre-training strategy as + *Pre-training*, which achieves an additional improvement of 2.26% in PSNR. These results demonstrate the effectiveness of each component of our method.

We demonstrate the effectiveness of our hypernetwork acceleration strategy via TABLE. III. It compares the per-

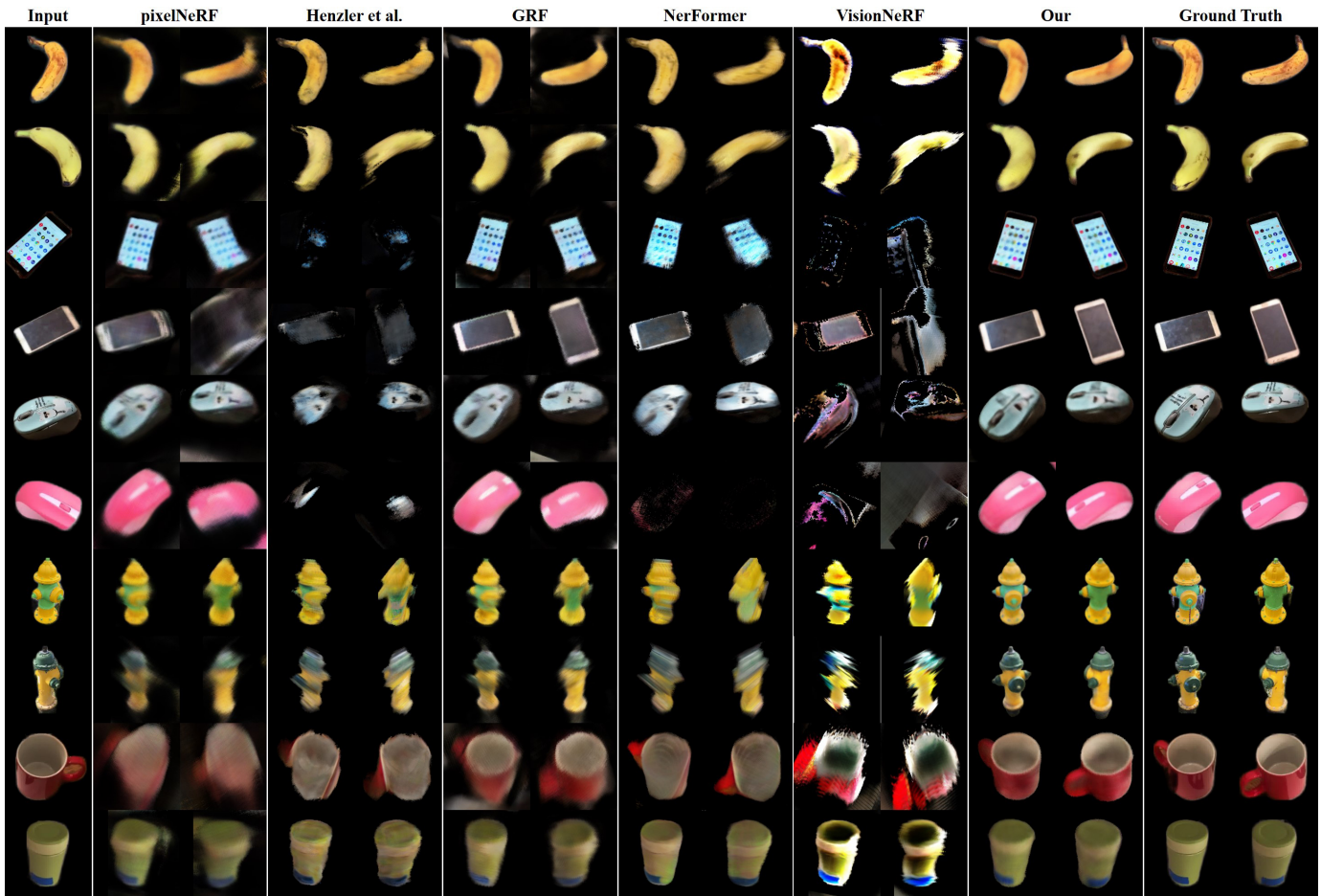


Fig. 8. Qualitative comparison with existing approaches. We reconstruct each instance using the input image and render two novel views for each instance. Two test samples are reported for each category.

TABLE II

ABLATION STUDY ON BANANA CATEGORY. WE ENABLE THE COMPONENTS ONE BY ONE TO DEMONSTRATE THEIR EFFECTIVENESS.

Method	PSNR \uparrow	SSIM \uparrow	LPIPS \downarrow
baseline	20.274	0.8169	0.2087
+ Template	19.3489	0.8076	0.2089
+ Alignment	22.2576	0.8535	0.1739
+ Multi-Level Feature	22.4797	0.8575	0.1694
+ Pre-training	22.9867	0.8607	0.1681

formance and inference speed of our method with the baseline method, denoted as *Direct*. The baseline method takes the latent representations z_d and z_c as additional input via concatenation to the deformation and color submodules of Φ_i , respectively. *Model Size* indicates the number of hidden neurons of each layer in these two submodules. Our method outperforms the baseline method in both reconstruction and inference speed. The reason is that our method uses hypernetworks to generate instance-specific Φ_i that only take point location as input, while the baseline method uses category-specific Φ_i that take additional inputs of z_d and z_c , which increases computational cost. Moreover, the generation of the hypernetworks is done only once for each instance, thus

TABLE III

QUANTITATIVE COMPARISON BETWEEN CATEGORY-SPECIFIC Φ_i (DIRECT) AND INSTANCE-SPECIFIC Φ_i (OUR). EXPERIMENT IS CONDUCTED ON HYDRANT CATEGORY.

Method	Model Size	Sec/Frame	PSNR \uparrow	SSIM \uparrow	LPIPS \downarrow
Direct	192	0.92	17.784	0.825	0.177
	512	2.06	18.392	0.838	0.168
	1280	7.76	18.783	0.841	0.166
Our	192	0.75	19.009	0.847	0.162

is time-efficient. As the model size increases, the baseline method improves its reconstruction performance but also slows down its inference speed. Our method achieves 1.20% higher PSNR than the baseline method with 1280 hidden neurons, while reducing the inference time by 90.45%.

E. Application

We demonstrate the application potential of our framework with three examples: shape interpolation, object synthesis and object placement. We will detail them in the next paragraphs.

Fig. 9 shows the shape interpolation example. Given a source image I_s and a target image I_t , and their foreground masks M_s and M_t , we encode them into latent geometry



Fig. 9. Shape interpolation. The objects in the middle box are synthesized using the appearance representations from the source objects and the geometry representations interpolated between the source and target objects.

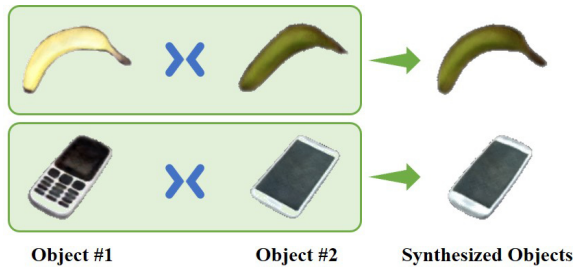


Fig. 10. Object synthesis. The objects on the right side are synthesized using the geometry representations from object #1 and the appearance representations from object #2.

representations z_d^s and z_d^t . Then, we interpolate them with a parameter λ to obtain a new latent representation $z_d' = \lambda \cdot z_d^s + (1 - \lambda) \cdot z_d^t$. We render the images using the new geometry representation z_d' and the appearance representation z_c^s of the source image.

Our method separates the geometry and appearance representations with z_d and z_c , respectively. This allows us to synthesize a new object by combining the latent representations of different object instances, as Fig. 10 illustrates. Given two images of different object instances of the same category, we encode them into latent representations. We use the geometry representation of the first instance, z_d^0 , and the appearance representation of the second instance, z_c^1 , to condition the deformation and color submodules of Φ_i , respectively, and render the synthesized object.

Our framework reconstructs the objects in a canonical (or template) space, which has a consistent coordinate system. This enables us to easily place different object instances into a single scene with arbitrary transformations, as Fig. 11 demonstrates. This application can also place object instances of different categories, and can be extended to construct more complex scenes by placing multiple and diverse objects.

V. LIMITATION AND FUTURE WORK

Here, we discuss some limitations of our current framework and outline some future directions to overcome them.

Firstly, our method creates the instance geometry by using a category-specific shape template and instance-specific deformations. We use the deformation submodule to predict a 3D translation for each point on the template. However, this strategy may not handle large deformations well. To

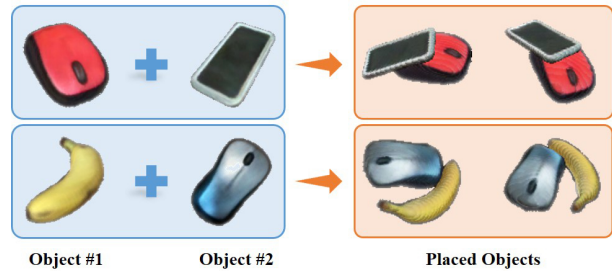


Fig. 11. Object placement. Our method reconstructs objects in a canonical space, which allow us to easily place different objects into a single scene.

address this, we plan to use an iterative prediction strategy for the deformation submodule. It would update and refine its predictions based on the current and previous states, and better model the large deformations.

Secondly, our framework is built on the original NeRF approach. We plan to incorporate recent improvements in NeRF-related fields, such as Mip-NeRF [53] and instant-ngp [54], to achieve better performance and faster training and inference speed.

VI. CONCLUSION

We propose VRF, an efficient framework that can reconstruct an object of a specific category from a single image without requiring any known camera parameters at inference time. Our framework uses global latent representations to model the geometry and appearance, which avoids the need for frequent access to local pixel features and camera parameters. To simplify the geometry, we use a category-specific shape template and deform it with instance-specific transformations. To enable semantic-consistent learning, we optimize a 3D similarity transformation that aligns each instance to the template space. Our framework outperforms existing methods in terms of performance and inference speed and demonstrates promising applications.

REFERENCES

- [1] J. Xie, Y. Chen, J. Liu, C. Miao, and X. Gao, "Interactive 3d caricature generation based on double sampling," in *ACM Multimedia*, 2009, p. 745–748.
- [2] Z. Tang, A. Patel, X. Guo, and B. Prabhakaran, "A multimodal virtual environment for interacting with 3d deformable models," in *ACM Multimedia*, 2011, p. 1009–1306.
- [3] Y. Guo, F. Sohel, M. Bennamoun, J. Wan, and M. Lu, "An accurate and robust range image registration algorithm for 3d object modeling," *IEEE Transactions on Multimedia*, vol. 16, no. 5, pp. 1377–1390, 2014.
- [4] S. An, S. Liu, Z. Huang, G. Che, Q. Bao, Z. Zhu, Y. Chen, and D. Z. Weng, "Rotaterview: A video composition system for interactive product display," *IEEE Transactions on Multimedia*, vol. 21, no. 12, pp. 3095–3105, 2019.
- [5] S. Wu, A. Makadia, J. Wu, N. Snavely, R. Tucker, and A. Kanazawa, "De-rendering the world's revolutionary artefacts," in *Proceedings of the IEEE/CVF conference on computer vision and pattern recognition*, 2021, pp. 6338–6347.
- [6] J. Gao, D. Kong, S. Wang, J. Li, and B. Yin, "Dasi: Learning domain adaptive shape impression for 3d object reconstruction," *IEEE Transactions on Multimedia*, pp. 1–15, 2022.
- [7] W. Nie, C. Jiao, R. Chang, L. Qu, and A.-A. Liu, "Cpg3d: Cross-modal priors guided 3d object reconstruction," *IEEE Transactions on Multimedia*, pp. 1–14, 2023.

- [8] B. Mildenhall, P. P. Srinivasan, M. Tancik, J. T. Barron, R. Ramamoorthi, and R. Ng, "Nerf: Representing scenes as neural radiance fields for view synthesis," in *European conference on computer vision*. Springer, 2020, pp. 405–421.
- [9] A. Yu, V. Ye, M. Tancik, and A. Kanazawa, "pixelnerf: Neural radiance fields from one or few images," in *Proceedings of the IEEE/CVF Conference on Computer Vision and Pattern Recognition*, 2021, pp. 4578–4587.
- [10] Q. Wang, Z. Wang, K. Genova, P. P. Srinivasan, H. Zhou, J. T. Barron, R. Martin-Brualla, N. Snavely, and T. Funkhouser, "Ibrnet: Learning multi-view image-based rendering," in *Proceedings of the IEEE/CVF Conference on Computer Vision and Pattern Recognition*, 2021, pp. 4690–4699.
- [11] A. Chen, Z. Xu, F. Zhao, X. Zhang, F. Xiang, J. Yu, and H. Su, "Mvsnerf: Fast generalizable radiance field reconstruction from multi-view stereo," in *Proceedings of the IEEE/CVF International Conference on Computer Vision*, 2021, pp. 14 124–14 133.
- [12] M. M. Johari, Y. Lepoittevin, and F. Fleuret, "Geonerf: Generalizing nerf with geometry priors," in *Proceedings of the IEEE/CVF Conference on Computer Vision and Pattern Recognition (CVPR)*, June 2022, pp. 18 365–18 375.
- [13] J. T. Kajiya and B. P. Von Herzen, "Ray tracing volume densities," *ACM SIGGRAPH computer graphics*, vol. 18, no. 3, pp. 165–174, 1984.
- [14] A. v. d. Oord, Y. Li, and O. Vinyals, "Representation learning with contrastive predictive coding," *arXiv preprint arXiv:1807.03748*, 2018.
- [15] T. Chen, S. Kornblith, M. Norouzi, and G. Hinton, "A simple framework for contrastive learning of visual representations," in *International conference on machine learning*. PMLR, 2020, pp. 1597–1607.
- [16] K. He, H. Fan, Y. Wu, S. Xie, and R. Girshick, "Momentum contrast for unsupervised visual representation learning," in *Proceedings of the IEEE/CVF conference on computer vision and pattern recognition*, 2020, pp. 9729–9738.
- [17] D. Ha, A. Dai, and Q. V. Le, "Hypernetworks," *arXiv preprint arXiv:1609.09106*, 2016.
- [18] J. Reizenstein, R. Shapovalov, P. Henzler, L. Sbordone, P. Labatut, and D. Novotny, "Common objects in 3d: Large-scale learning and evaluation of real-life 3d category reconstruction," in *Proceedings of the IEEE/CVF International Conference on Computer Vision*, 2021, pp. 10 901–10 911.
- [19] G. Yang, X. Huang, Z. Hao, M.-Y. Liu, S. Belongie, and B. Hariharan, "Pointflow: 3d point cloud generation with continuous normalizing flows," in *Proceedings of the IEEE/CVF International Conference on Computer Vision*, 2019, pp. 4541–4550.
- [20] G. Gkioxari, J. Malik, and J. Johnson, "Mesh r-cnn," in *Proceedings of the IEEE/CVF International Conference on Computer Vision*, 2019, pp. 9785–9795.
- [21] C. B. Choy, D. Xu, J. Gwak, K. Chen, and S. Savarese, "3d-r2n2: A unified approach for single and multi-view 3d object reconstruction," in *European conference on computer vision*. Springer, 2016, pp. 628–644.
- [22] M. Atzmon and Y. Lipman, "Sal: Sign agnostic learning of shapes from raw data," in *Proceedings of the IEEE/CVF Conference on Computer Vision and Pattern Recognition*, 2020, pp. 2565–2574.
- [23] S. Tulsiani, T. Zhou, A. A. Efros, and J. Malik, "Multi-view supervision for single-view reconstruction via differentiable ray consistency," in *Proceedings of the IEEE conference on computer vision and pattern recognition*, 2017, pp. 2626–2634.
- [24] A. Kar, C. Häne, and J. Malik, "Learning a multi-view stereo machine," *Advances in neural information processing systems*, vol. 30, 2017.
- [25] A. X. Chang, T. Funkhouser, L. Guibas, P. Hanrahan, Q. Huang, Z. Li, S. Savarese, M. Savva, S. Song, H. Su *et al.*, "Shapenet: An information-rich 3d model repository," *arXiv preprint arXiv:1512.03012*, 2015.
- [26] A. Kanazawa, S. Tulsiani, A. A. Efros, and J. Malik, "Learning category-specific mesh reconstruction from image collections," in *Proceedings of the European Conference on Computer Vision (ECCV)*, September 2018.
- [27] S. Goel, A. Kanazawa, and J. Malik, "Shape and viewpoint without keypoints," in *Computer Vision – ECCV 2020*, A. Vedaldi, H. Bischof, T. Brox, and J.-M. Frahm, Eds. Cham: Springer International Publishing, 2020, pp. 88–104.
- [28] S. Wu, T. Jakab, C. Rupprecht, and A. Vedaldi, "Dove: Learning deformable 3d objects by watching videos," *arXiv preprint arXiv:2107.10844*, 2021.
- [29] C. Xie, K. Park, R. Martin-Brualla, and M. Brown, "Fig-nerf: Figure-ground neural radiance fields for 3d object category modelling," in *2021 International Conference on 3D Vision (3DV)*. IEEE, 2021, pp. 962–971.
- [30] W. Jang and L. Agapito, "Codenerf: Disentangled neural radiance fields for object categories," in *Proceedings of the IEEE/CVF International Conference on Computer Vision*, 2021, pp. 12 949–12 958.
- [31] J. J. Park, P. Florence, J. Straub, R. Newcombe, and S. Lovegrove, "Deepsdf: Learning continuous signed distance functions for shape representation," in *Proceedings of the IEEE/CVF Conference on Computer Vision and Pattern Recognition*, 2019, pp. 165–174.
- [32] D. Rebain, M. Matthews, K. M. Yi, D. Lagun, and A. Tagliasacchi, "Lolnerf: Learn from one look," in *Proceedings of the IEEE/CVF Conference on Computer Vision and Pattern Recognition*, 2022, pp. 1558–1567.
- [33] A. Jain, M. Tancik, and P. Abbeel, "Putting nerf on a diet: Semantically consistent few-shot view synthesis," in *Proceedings of the IEEE/CVF International Conference on Computer Vision*, 2021, pp. 5885–5894.
- [34] K. Deng, A. Liu, J.-Y. Zhu, and D. Ramanan, "Depth-supervised nerf: Fewer views and faster training for free," in *Proceedings of the IEEE/CVF Conference on Computer Vision and Pattern Recognition*, 2022, pp. 12 882–12 891.
- [35] B. Roessle, J. T. Barron, B. Mildenhall, P. P. Srinivasan, and M. Nießner, "Dense depth priors for neural radiance fields from sparse input views," in *Proceedings of the IEEE/CVF Conference on Computer Vision and Pattern Recognition*, 2022, pp. 12 892–12 901.
- [36] D. Chen, Y. Liu, L. Huang, B. Wang, and P. Pan, "Geoaug: Data augmentation for few-shot nerf with geometry constraints," in *Computer Vision–ECCV 2022: 17th European Conference, Tel Aviv, Israel, October 23–27, 2022, Proceedings, Part XVII*. Springer, 2022, pp. 322–337.
- [37] D. Xu, Y. Jiang, P. Wang, Z. Fan, H. Shi, and Z. Wang, "Sinnerf: Training neural radiance fields on complex scenes from a single image," in *Computer Vision–ECCV 2022: 17th European Conference, Tel Aviv, Israel, October 23–27, 2022, Proceedings, Part XXII*. Springer, 2022, pp. 736–753.
- [38] A. Trevisethick and B. Yang, "Grf: Learning a general radiance field for 3d representation and rendering," in *Proceedings of the IEEE/CVF International Conference on Computer Vision*, 2021, pp. 15 182–15 192.
- [39] P. Henzler, J. Reizenstein, P. Labatut, R. Shapovalov, T. Ritschel, A. Vedaldi, and D. Novotny, "Unsupervised learning of 3d object categories from videos in the wild," in *Proceedings of the IEEE/CVF Conference on Computer Vision and Pattern Recognition*, 2021, pp. 4700–4709.
- [40] J. Chibane, A. Bansal, V. Lazova, and G. Pons-Moll, "Stereo radiance fields (srf): Learning view synthesis for sparse views of novel scenes," in *Proceedings of the IEEE/CVF Conference on Computer Vision and Pattern Recognition*, 2021, pp. 7911–7920.
- [41] K.-E. Lin, Y.-C. Lin, W.-S. Lai, T.-Y. Lin, Y.-C. Shih, and R. Ramamoorthi, "Vision transformer for nerf-based view synthesis from a single input image," in *Proceedings of the IEEE/CVF Winter Conference on Applications of Computer Vision*, 2023, pp. 806–815.
- [42] A. M. Andrew, "Multiple view geometry in computer vision," *Kybernetes*, 2001.
- [43] Z. Zheng, T. Yu, Q. Dai, and Y. Liu, "Deep implicit templates for 3d shape representation," in *Proceedings of the IEEE/CVF Conference on Computer Vision and Pattern Recognition*, 2021, pp. 1429–1439.
- [44] Z. Wang, A. C. Bovik, H. R. Sheikh, and E. P. Simoncelli, "Image quality assessment: from error visibility to structural similarity," *IEEE transactions on image processing*, vol. 13, no. 4, pp. 600–612, 2004.
- [45] R. Zhang, P. Isola, A. A. Efros, E. Shechtman, and O. Wang, "The unreasonable effectiveness of deep features as a perceptual metric," in *Proceedings of the IEEE conference on computer vision and pattern recognition*, 2018, pp. 586–595.
- [46] A. Paszke, S. Gross, S. Chintala, G. Chanan, E. Yang, Z. DeVito, Z. Lin, A. Desmaison, L. Antiga, and A. Lerer, "Automatic differentiation in pytorch," 2017.
- [47] N. Ravi, J. Reizenstein, D. Novotny, T. Gordon, W.-Y. Lo, J. Johnson, and G. Gkioxari, "Accelerating 3d deep learning with pytorch3d," *arXiv:2007.08501*, 2020.
- [48] K. He, X. Zhang, S. Ren, and J. Sun, "Deep residual learning for image recognition," in *Proceedings of the IEEE conference on computer vision and pattern recognition*, 2016, pp. 770–778.
- [49] S. Ioffe and C. Szegedy, "Batch normalization: Accelerating deep network training by reducing internal covariate shift," in *International conference on machine learning*. pmlr, 2015, pp. 448–456.
- [50] Y. Zhou, C. Barnes, J. Lu, J. Yang, and H. Li, "On the continuity of rotation representations in neural networks," in *Proceedings of the IEEE/CVF Conference on Computer Vision and Pattern Recognition*, 2019, pp. 5745–5753.

- [51] D.-A. Clevert, T. Unterthiner, and S. Hochreiter, “Fast and accurate deep network learning by exponential linear units (elus),” *arXiv preprint arXiv:1511.07289*, 2015.
- [52] D. P. Kingma and J. Ba, “Adam: A method for stochastic optimization,” *arXiv preprint arXiv:1412.6980*, 2014.
- [53] J. T. Barron, B. Mildenhall, M. Tancik, P. Hedman, R. Martin-Brualla, and P. P. Srinivasan, “Mip-nerf: A multiscale representation for anti-aliasing neural radiance fields,” in *Proceedings of the IEEE/CVF International Conference on Computer Vision*, 2021, pp. 5855–5864.
- [54] T. Müller, A. Evans, C. Schied, and A. Keller, “Instant neural graphics primitives with a multiresolution hash encoding,” *ACM Transactions on Graphics (ToG)*, vol. 41, no. 4, pp. 1–15, 2022.